RESEARCH ARTICLE

Check for updates

Guarding the heterogeneous interface of perovskite solar cells by the anion-barrier synthesized using residual PbI₂†

Wenqi Zeng,‡[a] Zezhuan Jiang, [ID] ‡[a] Xiaofeng He,[a] Limin Lai,[a] Jiayu You,[e] Gaobo Xu,[a] Hongyu Bian,[a,b] Cunyun Xu,*[a] Zhongjun Dai,[a] Sam Zhang [ID] *[c,d] and Qunliang Song [ID] *[a]

Ion migration and diffusion, particularly in the case of halide ions, are among the bottlenecks of the efficiency and stability of perovskite solar cells (PSCs). The residue of lead iodide (PbI₂) is easily produced by the spin-coating deposition of the perovskite film, which introduces more uncertainty to the active layer and even leads to adverse effects across the interface. In this study, a clever strategy of *in situ* synthesis anion-barrier was used to lock the iodide ions at the heterogeneous interface. The solution is to convert the residual PbI₂ into δ-CsPbI₃, which is more capable to bind iodine. These *in situ* synthesized δ-CsPbI₃ not only blocked the diffusion of iodide ions into Spiro-OMeTAD but also promoted the energy level alignment about 0.3 eV between perovskite and Spiro-OMeTAD. Fortunately, this also improved the quality of the active layer. In the end, the device based on *in situ* synthesized anion-barrier achieved an increased power conversion efficiency (PCE) of 21.21% from 19.62% of the reference without such a treatment. Meanwhile, the stability of the treated PSCs maintained 88.2% of their initial PCE after being stored for about 1200 h under dark conditions and controlled RH of 15–25%. This study provides a new solution and technical reference for the inhibition of ion diffusion in PSCs.

1. Introduction

Due to the advantages of perovskite materials, such as low cost, adjustable band gap and long carrier diffusion length, perovskite solar cells (PSCs) have flourished rapidly in the past decade and attracted the attention of many researchers.[1–4] Single-junction PSCs have reached the highest power conversion efficiency (PCE) of 26.1%,[5,6] and many bottlenecks still need to be addressed in order to achieve faster commercialization. Ion migration and diffusion are among the key factors affecting the performance

and stability of PSCs. In particular, in normal devices, anion diffusion has seriously restricted their applications.

Most of the organic–inorganic hybrid perovskite films are deposited by the solution method and then annealed to achieve crystal phase transformation. It is difficult to avoid residual lead iodide (PbI₂) in the active layers due to the difference in the escape temperature of each component.[7,8] The bad effect has been confirmed by numerous reports. For example, Adachi *et al.*[9,10] found that perovskite films would be seriously degraded under light, forming metallic lead (Pb⁰) and iodine elements due to the existence of PbI₂. Deep level defects were introduced because of the reduced trap activation energy, degrading the perovskite films and reducing the device stability.[11,12] In addition, because of the potential difference between the perovskite and Spiro-OMeTAD, the charge transport was seriously reduced, resulting in the loss of open circuit voltage (V_{OC}).[13] The introduction of a heterojunction can greatly improve this situation. Li *et al.*[14] introduced a δ-FAPbI₃ heterojunction on top of the perovskite to better match the energy levels between the perovskite and Spiro-OMeTAD, finally increasing the V_{OC} value from 1.12 to 1.16 V. Similarly, other researchers have achieved these energy level adjustments by introducing foreign functional molecules or dopants such as NDAPBF₄[15] and PETA-G.[16] However, energy level regulation

[a]*Institute for Clean Energy and Advanced Materials, School of Materials and Energy, Southwest University, Chongqing 400715, China. E-mail: cyxuamos@foxmail.com, qlsong@swu.edu.cn*

[b]*Center for Advanced Thin Films and Devices, School of Materials and Energy, Southwest University, Chongqing 400715, P. R. China*

[c]*School of Aeronautics, Harbin Institute of Technology, Harbin 150001, China. E-mail: samzhang@hit.edu.cn*

[d]*Zhengzhou Research Institute, Harbin Institute of Technology, Zhengzhou 450000, China*

[e]*College of Materials Science and Engineering, Sichuan University, Chengdu 610064, Sichuan, China*

†Electronic supplementary information (ESI) available. See DOI: https://doi.org/10.1039/d4qi00327f

‡These authors contributed equally to this work.

This journal is © the Partner Organisations 2024

Inorg. Chem. Front., 2024, **11**, 5137–5146 | **5137**

alone cannot solve all problems. Another trouble particularly prominent in PSCs is lattice defects and even the rapid degradation of the active layer caused by the migration of halide ions.[17,18] The void of iodine forms defects in perovskites, and the escaping iodine ions would diffuse to the Spiro-OMeTAD layer and react with it. According to a report,[19] Spiro-OMeTAD$^+$ can interact with iodine ions to irreversibly reduce the electrical conductivity of Spiro-OMeTAD. The iodide ions diffused out of Spiro-OMeTAD can also react with the Ag electrode.[20,21] The iodide-induced formation of silver iodide would continuously degrade the perovskite films and ultimately reduce the device stability. Clearly, the residual PbI_2 not only affects the contact interface but also provides a channel for ion migration or diffusion. It is very hard to solve these problems simultaneously, and the reported work only focused on how to reduce PbI_2.[22,23] It is difficult to block halide ions without affecting the charge transport.

In this study, a strategy of *in situ* chemical reaction to construct the anion-barrier is proposed to optimize the heterogeneous interface between the active layer and hole transport layer (HTL), consuming the residual PbI_2 generated by solution deposition. The PbI_2 on the perovskite are converted into δ-$CsPbI_3$ with higher stability, which can improve the energy alignment between the perovskite film and HTL to enhance the V_{OC}. The formation of δ-$CsPbI_3$ effectively made up for the deficiency of iodide ion and resisted the diffusion of iodine ions from the perovskite to Spiro-OMeTAD. δ-$CsPbI_3$ also improved the surface hydrophobicity of the perovskite films to increase the device stability. Finally, the quality of both perovskite and Spiro-OMeTAD films was improved. The stability and efficiency of the sample after the introduction of the anion-barrier were significantly improved. These results will provide new solutions and technical references for the inhibition of ion diffusion.

2. Results and discussion

2.1. *In situ* synthesis and influence

The fabrication process and interaction mechanism of the double-layer structure of perovskite/δ-$CsPbI_3$ is shown in Fig. 1. The residual PbI_2 during the preparation of perovskite can be converted into δ-$CsPbI_3$ by reacting with Cs–I precursor solution. In order to confirm that the Cs–I treatment can reduce the residual PbI_2 in the perovskite film, a higher concentration of Cs–I precursor was used, and the X-ray diffraction (XRD) patterns were used to determine the final products. The sample prepared using PbI_2 and Cs–I precursor solution with equal molar ratio was obtained after annealing at 60 °C for 10 min. As shown in Fig. 2a, eight peaks appeared at 7.17°, 9.87°, 11.24, 25.64°, 26.27°, 27.02°, 29.24°, and 31.20°, respectively, compared to the material from the Cs–I precursor and substrate (Fig. S1a†). According to the literature reported,[24,25] these peaks come from δ-$CsPbI_3$. The XRD patterns of the
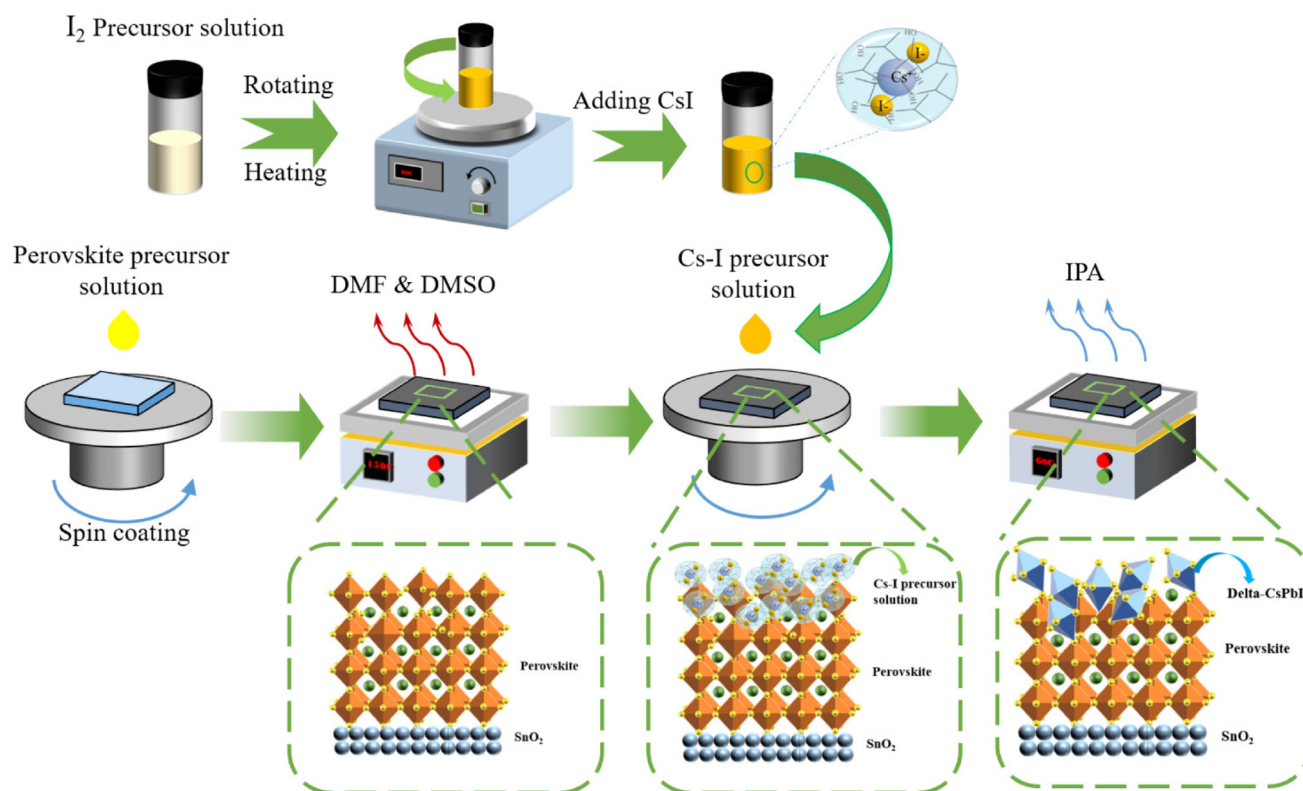

Fig. 1 Schematic illustrations of the fabrication process and interaction mechanism for the perovskite and Cs−I precursor solution.
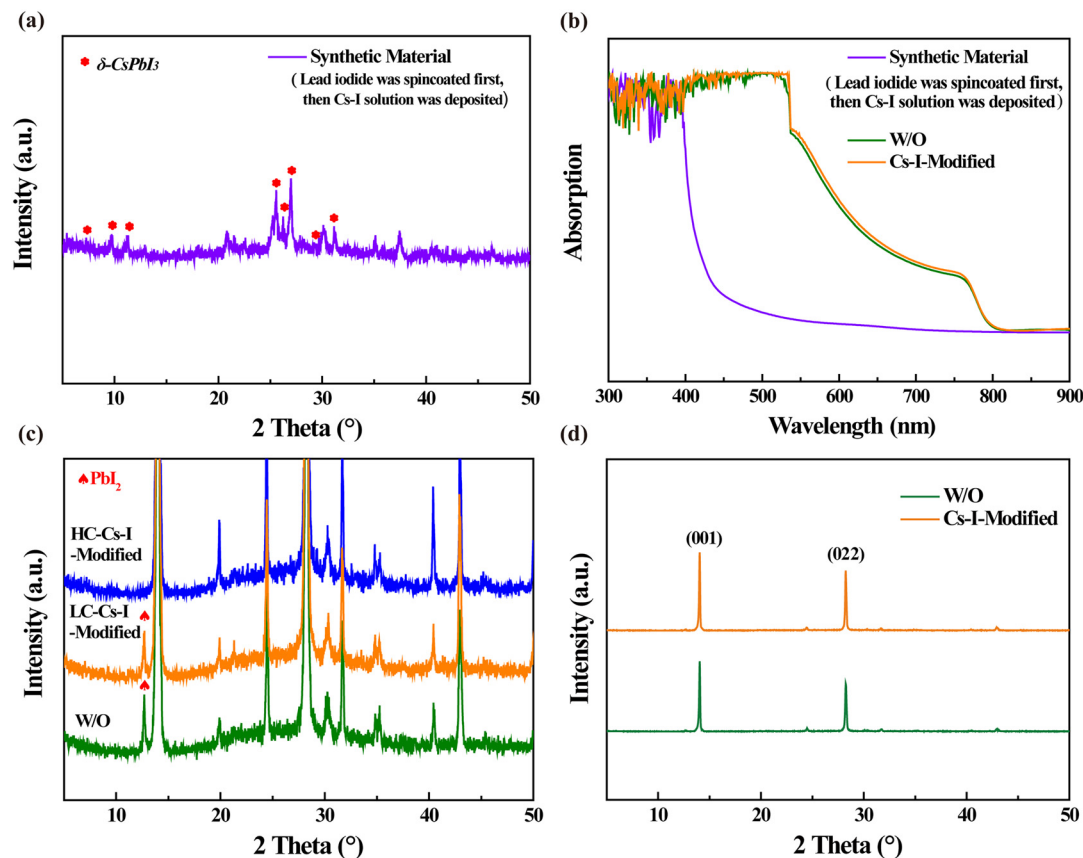
5138 | *Inorg. Chem. Front.*, 2024, 11, 5137–5146

This journal is © the Partner Organisations 2024

Fig. 2 (a) XRD patterns of the samples by reacting PbI_2 with equal molar Cs–I precursor solution; (b) UV–visible absorption spectra of the synthetic material, W/O and Cs–I-modified samples. XRD patterns for (c) the reference and films treated with low and high concentrations of the Cs–I precursor and (d) the W/O and Cs–I-modified perovskite films.

samples by reacting PbI_2 with equal molar Cs–I precursor solution at different annealing times are obtained as shown in Fig. S1b,† indicating that there is no transformation process from α-$CsPbI_3$ to δ-$CsPbI_3$. Further verification of the UV-visible absorption spectra is shown in Fig. 2b, which is consistent with that of the δ-$CsPbI_3$ film in the literature.[26] Fig. 2c show the results of XRD measurements of three samples with different concentrations of Cs–I precursors. Compared with the reference sample without Cs–I treatment (W/O), the peak at 12.7° belongs to PbI_2. The PbI_2 content decreases in low Cs–I concentration (0.15 mg mL^{-1}, named LC–Cs–I-modified) treated sample and completely disappears in high Cs–I concentration sample (0.5 mg mL^{-1}, named HC–Cs–I-modified). The disappearance of PbI_2 and the above-mentioned results confirm that the Cs–I precursor solution reacts with residual PbI_2 to form δ-$CsPbI_3$. In addition, the cooperation of Cs$^+$ with the bulk phase of the perovskite can be confirmed by the two diffraction peaks of (001) and (022), moving to a higher angle at high concentration Cs–I treatment, as shown in Fig. S1c and d.†

For studying the effect of Cs–I precursor solution on the crystallization of perovskite films, XRD comparison was performed on the optimal concentration Cs–I modified (Cs–I-modified, 0.15 mg mL^{-1}) and unmodified (W/O) perovskite films. As shown in Fig. 2d, the diffraction peaks of both the

samples are almost the same. The two main peaks (001) and (022) are at 14.03° and 28.25°, respectively, indicating the not affected lattice of the perovskite.[27,28] However, the peak intensities of the (001) and (022) peaks are enhanced after Cs–I modification, which can be attributed to the better crystallinity with reduced defects,[29] as will be demonstrated later. The full width at half maximum (FWHM) of the three diffraction peaks is given in Table S1.† The unchanged FWHM at the (001) plane implies that the grain size of the perovskite film is hardly changed by Cs–I treatment. The higher UV-visible absorption spectra shown in Fig. 2b is another advantage of the Cs–I treatment.

The top-view scanning electron microscopy (SEM) images compared in Fig. S2a and b† show generally small morphology difference between the reference and Cs–I-modified perovskite films. The much smaller nanoparticles marked by red circles of the Cs–I-modified film are believed to be δ-$CsPbI_3$ particles. Furthermore, the cross-sectional SEM images shown in Fig. S2c and d† show little change, which is similar to those reported before.[30]

2.2. Interfacial anion barrier and optimization

X-ray photoelectron spectroscopy (XPS) measurements were performed to confirm the interaction between the Cs–I precur-

This journal is © the Partner Organisations 2024

Inorg. Chem. Front., 2024, **11**, 5137–5146 | **5139**

sor solution and perovskite or Spiro-OMeTAD. As shown in Fig. 3a and b and listed in Table S2,† the binding energy peaks of Pb 4f$_{7/2}$ and Pb 4f$_{5/2}$ after Cs–I modification shift toward higher binding energies of 136.92 and 141.82 eV, respectively, 0.1 eV larger than the reference ones. These shifts indicate the formation of δ-CsPbI$_3$ because the binding energy of Pb^{2+} in δ-CsPbI$_3$[31] is higher than that in FAPbI$_3$.[32] At the same time, the core-level spectra of I 3d for W/O and Cs–I-modified perovskite films are shown in Fig. 3c and listed in Table S2.† The almost unchanged binding energy values are consistent with the structure of PbI$_3^-$ in δ-CsPbI$_3$. Fig. 3d shows the typical I 3d signals in the Spiro-OMeTAD film without Cs–I modification, which is believed to be caused by the diffusion of iodide ions from the perovskite. These diffused iodide ions will eventually react with Spiro-OMeTAD to reduce its electrical conductivity and can further react with silver electrodes to form silver iodide[21] to reduce the device stability. After Cs–I precursor solution modification, no iodine signals are detected on the surface of the Spiro-OMeTAD film, as shown in Fig. 3d. The *in situ* synthetic δ-CsPbI$_3$ prevents the diffusion of iodine ions to the Spiro-OMeTAD film.

The energy dispersive spectroscopy (EDS) spectrum, as shown in Fig. S3a–c,† shows the uniform distribution of lead, iodine, and cesium. This shows that the Cs–I precursor solution can distribute uniformly on the surface of the perovskite.

According to reports,[33] PbI$_2$ is normally located on the top of the perovskite films.

Atomic force microscopy[34] (AFM) was carried out to study the effect of the Cs–I precursor solution on the surface morphology of the perovskite films. As shown in Fig. S4a and b,† the Root Mean Square (RMS) of the pristine perovskite film (W/O) is slightly reduced from 39.5 to 31.0 nm after Cs–I precursor solution treatment. This can be attributed to the formed δ-CsPbI$_3$ by recrystallization to fill the concave of the surface of the perovskite at the moment of preparation. Furthermore, the contact angles were obtained by contact angle measurements (Fig. S4c and d†). The water contact angle measurements[35,36] increase from 55.56 to 64.42°, demonstrating better hydrophobicity after introducing the Cs–I precursor solution. The better hydrophobicity of the Cs–I-modified treatment will then be beneficial to the higher stability of the perovskite film.

Not limited to the improvement of the crystallinity of perovskite films, the positive contribution to the energy level alignment is further confirmed by ultraviolet photoelectron spectroscopy (UPS).[37] As shown in Fig. 4a and b, the Fermi edge ($E_{F,edge}$) and the cut-off binding energies (E_{cutoff}) of the perovskite film without modification (W/O) are 1.50 and 16.22 eV, respectively, while the two values are shifted to higher values of 1.53 and 16.57 eV, respectively (Fig. 4c and d),
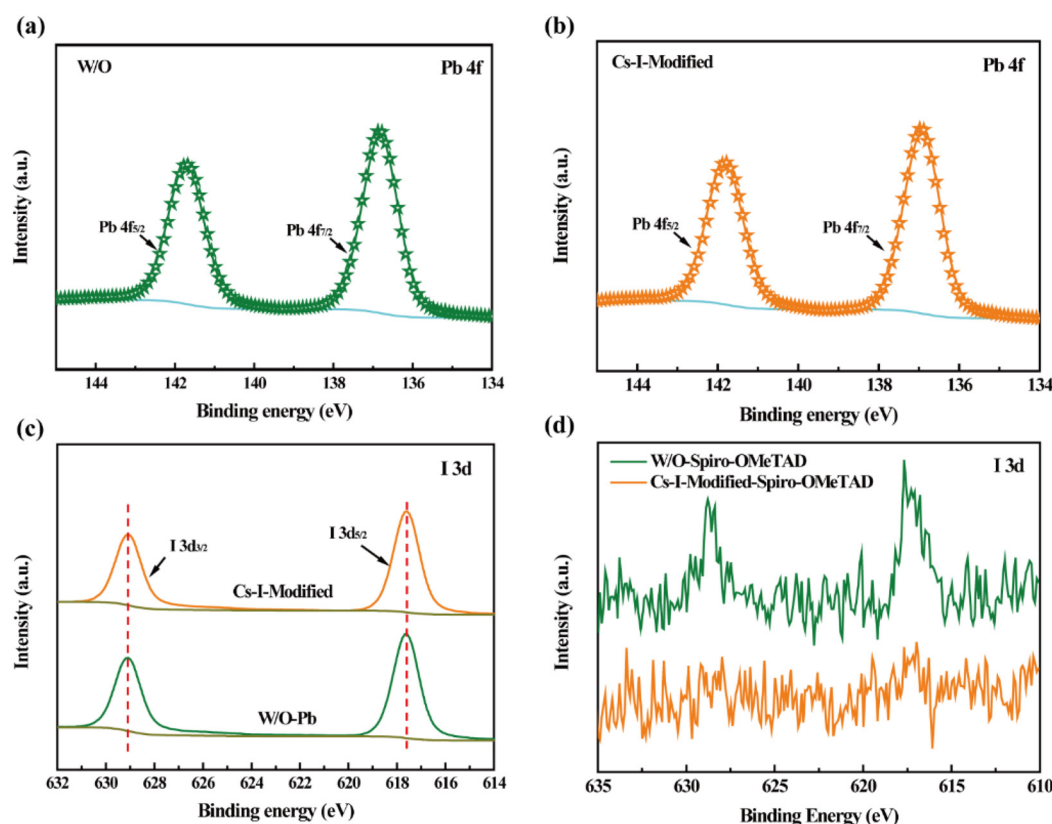

Fig. 3 XPS results of the Pb 4f spectra of perovskite films (a) without and (b) with Cs–I precursor treatment. The comparison of I 3d signals without and with Cs–I precursor treatment (c) on perovskite films and (d) on Spiro-OMeTAD films.

5140 | *Inorg. Chem. Front.*, 2024, **11**, 5137–5146

This journal is © the Partner Organisations 2024

after Cs–I modification. Based on the band gap (E_g) acquired from the $(\alpha h\nu)^2$ *versus* photon energy shown in Fig. S5a,† the E_g of both perovskite films is determined to be 1.56 eV. According to the formula,[38–40] the conduction band minimum (CBM) and valence band maximum (VBM) are calculated to be −4.94 and −6.5 eV, −4.53 and −6.22 eV, respectively, for the reference and the film after modification (Fig. 4e). The lower VBM value for the Cs–I-modified perovskite film matches Spiro-OMeTAD better, which is conducive to hole transport and increases the V_{OC}.

Generally speaking, the greater the built-in potential, the greater the driving force of charge transmission,[41,42] which can be more conducive to charge transmission and carrier collection. Indeed, the result of the Mott–Schottky curve measurement displayed in Fig. S5b† shows a larger built-in potential after Cs–I modification (0.95 compared 0.90 V of the reference), which is beneficial for achieving higher V_{OC}.

2.3. Device construction and characteristics

Subsequently, the samples with structures of Quartz/pristine PVSK/Spiro-OMeTAD and Quartz/Cs–I-modified PVSK/Spiro-OMeTAD were used to conduct steady-state photoluminescence (PL) and time-resolved photoluminescence (TRPL) measurements. The lower PL intensity of Cs–I-modified PVSK shown in Fig. 4f may be caused by two possibilities. The first is due to the enhancement of carrier extraction and transport at the interface, and the second is the increased trap defects in the perovskite film.[43] According to the above discussion, the fewer defects after Cs–I precursor treatment concludes that the reduction of the PL intensity is attributed to the better carrier extraction and transport. The TRPL measurements shown in Fig. 4g further confirms this conclusion. The fast and slow decay lifetimes (τ_1 and τ_2) obtained through bi-exponential fitting and then the calculated average decay lifetime (τ_{ave})[44,45] are listed in Table S3.† The smaller lifetimes of the Cs–I-modified perovskite sample (τ_{ave}, τ_1, and τ_2 are 143.96, 50.11, 195.17 ns, respectively) than those of the pristine perovskite sample (τ_{ave}, τ_1, and τ_2 are 238.11, 73.73, 282.73 ns, respectively) is the indicator of more efficient hole extraction, which is mainly ascribed to the more matched energy levels between the perovskite and Spiro-OMeTAD.

The two hole-only devices with the structures of ITO/PEDOT:PSS/pristine or Cs–I-modified perovskite/PTAA/MoO$_3$/Ag were fabricated to estimate the defect concentrations by the Space Charge-Limited Current (SCLC) method. The dark J–V curves of the two devices shown in Fig. 5a and b give the trap-filling limited voltage (V_{TFL}) of 0.378 and 0.132 V, respectively. Then, the defect density of ITO/PEDOT:PSS/perovskite/PTAA/MoO$_3$/Ag is calculated to be 6.19×10^{15} cm^{-3}, much larger than that of the ITO/PEDOT:PSS/Cs–I-modified perovskite/PTAA/MoO$_3$/Ag of 2.03×10^{15} cm^{-3}. This is consistent with the results in the previous section. The reduction of defects can help charge transportation, thereby increasing the capture efficiency of the carrier.[46–48]

The effects of Cs–I modification on charge transportation and carrier lifetime were further investigated by Transient Photocurrent (TPC) and Transient Photovoltage (TPV) measurements. As exhibited in Fig. 5c and d, the TPC value of
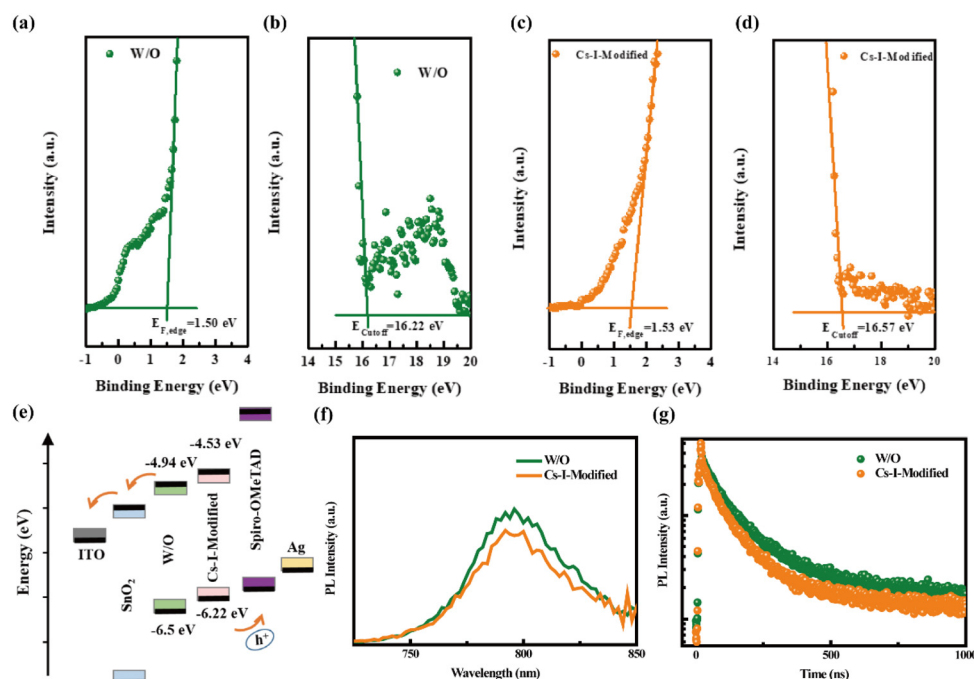

Fig. 4 The UPS spectra showing the E_{cutoff} and $E_{F,edge}$ of (a), (b) the W/O film; (c) and (d) the Cs–I-modified film; (e) energy level diagram of device components. (f) PL spectra and (g) time-resolved PL spectra for the samples of Quartz/pristine PVSK/Spiro-OMeTAD and Quartz/Cs–I-modified PVSK/Spiro-OMeTAD.
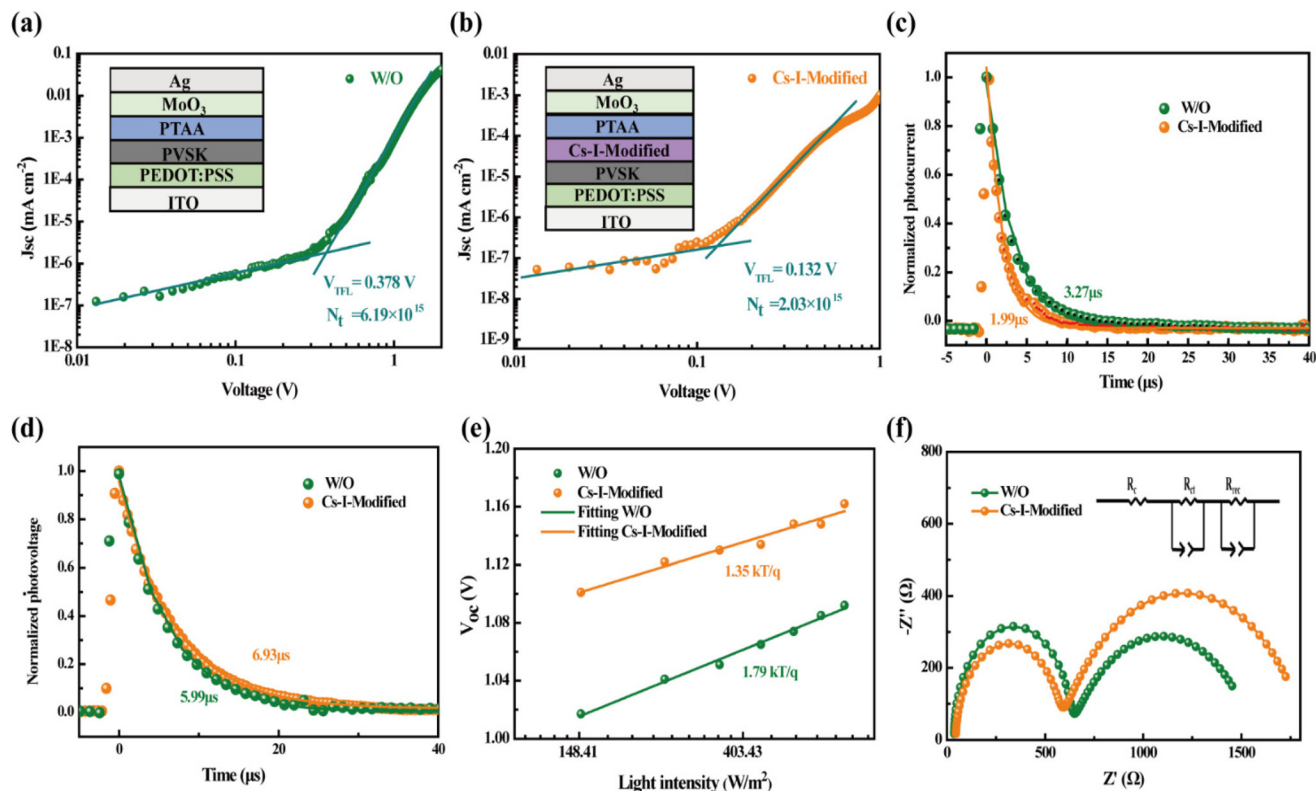
Fig. 5 Dark J–V curves of the hole-only devices with the structures of (a) ITO/PEDOT:PSS/Perovskite/PTAA/MoO$_3$/Ag and (b) ITO/PEDOT:PSS/Cs–I-modified Perovskite/PTAA/MoO$_3$/Ag. (c) TPC and (d) TPV decay curves, (e) V_{OC} as a function of light intensities, and (f) Nyquist plots of the PSCs without and with Cs–I modification.

3.27 µs is reduced to 1.99 µs after Cs–I modification. The lower the photocurrent decays, the better the carrier extraction obtained. The TPV tests show the longer photovoltage decay (6.93 µs) than that without Cs–I modification (5.99 µs), which can be attributed to the lower defect density mentioned above. To rule out other shunt channels for the shorter TPC after Cs–I modification, the ideal factor (n) was derived under different light intensities (I). The relationship between V_{OC} and I can be represented by the following eqn (1).[49]

$$\frac{\partial V_{OC}}{\partial(\ln I)} = \frac{nKT}{q} \qquad (1)$$

The value of n is generally between 1 (radiative recombination dominated) and 2 (non-radiative recombination dominated). The smaller n indicates the smaller defect-assisted non-radiative recombination.[50] As shown in Fig. 5e, the smaller n of 1.35 than that of the device without modification (n = 1.79) confirms that the defect assisted non-radiative recombination is reduced in the Cs–I-modified device.

Electrochemical impedance spectroscopy (EIS)[51] is an important characterization method to measure interfacial charge transport and defect recombination. As shown in Fig. 5f, the fitted parameters of the series impedance (R_s), the charge transfer and transport resistance (R_{ct}), and the recombi-

nation resistance (R_{rec}) are listed in Table S4.† The R_s of the Cs–I-modified device is slightly larger and is explained by the formation of δ-CsPbI$_3$ on the perovskite, resulting in slightly poor contact. The R_{ct} is reduced from 587.6 to 524.3 Ω after Cs–I modification, which is mainly attributed to better quality perovskite films and the better matching of energy levels. Compared with devices without treatment, the larger R_{rec} of Cs–I-modified devices indicates the reduction of defect states, which is beneficial to reduce the non-radiative recombination in the perovskite film.

The photoelectric performance of the devices with the perovskite films modified by different concentrations of Cs–I solutions are shown in Fig. S6a–d.† An obvious volcanic curve is observed at a concentration of 0.15 mg mL^{-1}. The performance decrease at a higher concentration of Cs–I solution can be ascribed to the large amount of δ-CsPbI$_3$ to increase the R_s in devices. As shown in Fig. 6a, the optimal Cs–I-modified device shows a PCE of 21.21%, V_{OC} of 1.184 V, short-circuit current density (J_{SC}) of 22.472 mA cm^{-2} and fill factor (FF) of 79.74%, respectively, while the optimal PCE of the reference device is 19.62%. The V_{OC}, J_{SC} and FF of the reference are 1.137 V, 22.049 mA cm^{-2} and 78.31%, respectively. The V_{OC} increase of the Cs–I-modified devices is mainly due to the better energy level matching and the increase of the built-in potential. The higher J_{SC} and FF are mainly attributed to the better quality of
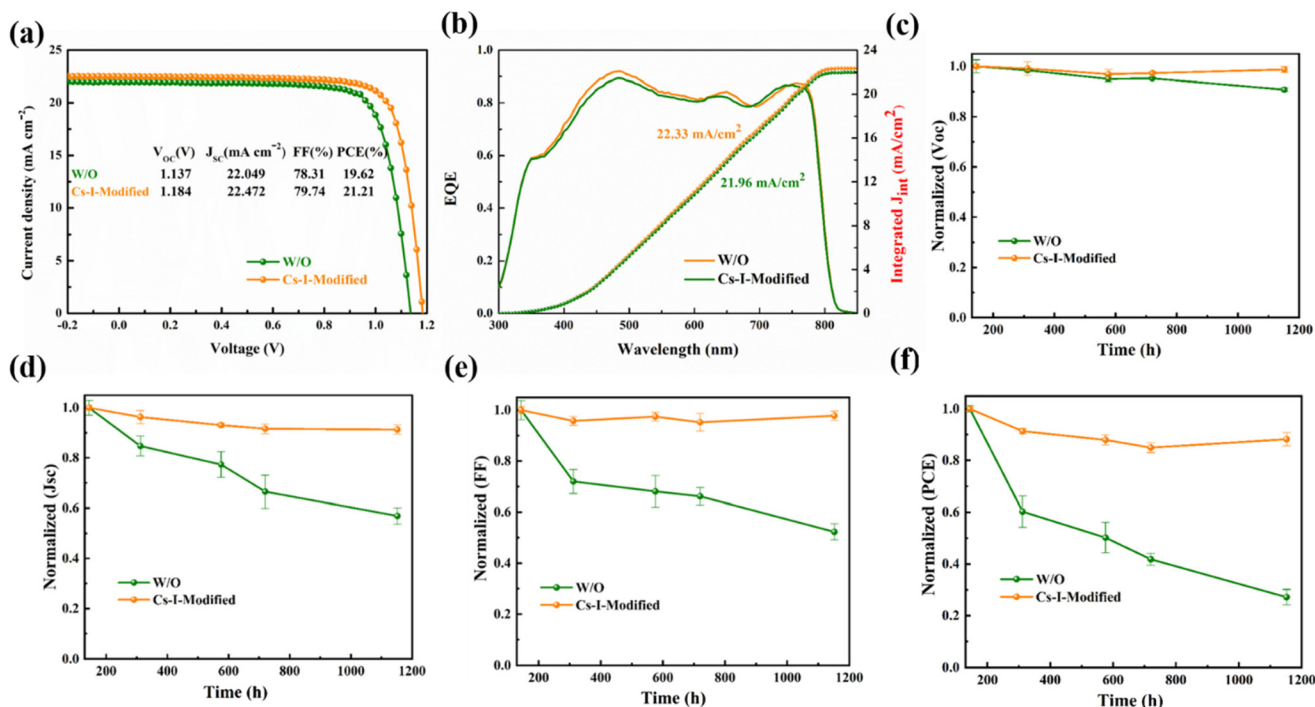
5142 | *Inorg. Chem. Front.*, 2024, **11**, 5137–5146

This journal is © the Partner Organisations 2024

Fig. 6 (a) Comparison of J–V curves of the champion devices and their (b) EQE and corresponding integrated J_{int} curves. The stability comparison of (c) V_{OC}, (d) J_{SC}, (e) FF, and (f) PCE of unencapsulated devices kept in the dark under a humidity of 15–25% RH at room temperature.

perovskite and the better interface charge extraction of Spiro-OMeTAD. The external quantum efficiency (EQE) measurements shown in Fig. 6b confirm the J–V measurements, showing the integrated currents of 21.96 and 22.33 mA cm^{-2} for the reference and the modified device, respectively. Besides the enhanced device performance, the reproducibility Cs–I-modified devices have been improved dramatically, as shown in Fig. S7.†

The forward scanning (FS) and reverse scanning (RS) measurements shown in Fig. S8a and b† give the hysteresis index (HI) according to the following eqn (2).

$$HI = \frac{PCE_{Reverse} - PCE_{Forward}}{PCE_{Reverse}} \quad (2)$$

The photovoltaic parameters under the FS and RS scanning directions are shown in Table S5.† The HI of Cs–I modified and control devices are 0.01 and 0.017, respectively. The stabilized power output of PSCs was measured at the maximum power point (MPP) under bias voltages of 0.968 V for the two devices under simulated AM 1.5G illumination of 100 mW cm^{-2}. As displayed in Fig. S8c and d,† both samples with and without Cs–I modification show stable output.

Finally, the long-term stability measurements of the unencapsulated were carried out under the conditions of a relative humidity (RH) of 15–25% at room temperature. The initial device performance was normalized to 20.36% of the Cs–I-modified device and 19.00% of the control device, respectively. As shown in Fig. 6c–f, the V_{OC}, J_{SC}, FF, and PCE for the control PSCs decay faster than the Cs–I-modified devices in about

1200 h. The PCE of the Cs–I-modified device can maintain about 88.2% of the initial PCE within this duration. Further thermal stability of the unencapsulated devices tested under elevated temperature (65 °C) for 120 h (Fig. S9a†) shows much better thermal stability of the Cs–I modified device. In addition, we have also explored the device stability under continuous illumination at ambient humidity (~20% RH). As shown in Fig. S9b,† the device based on Cs–I Modification also shows better photostability for 96 h continuous illumination. This better stability of Cs–I-modified devices can mainly synergistically be attributed to the reduction of PbI$_2$ on the perovskite, passivation of device defects, a more stable and hydrophobic δ-CsPbI$_3$, and better film quality of Spiro-OMeTAD by preventing the iodide ions from crossing the interface.

3. Conclusions

In summary, we used a clever strategy of *in situ* transfer waste PbI$_2$ into anion-barrier applying Cs–I precursor solution. First, superfluous PbI$_2$ reacted with Cs–I precursor solution to form δ-CsPbI$_3$, which is more hydrophobic and more stable, reducing ion diffusion through the heterogeneous interface. The δ-CsPbI$_3$ on the surface of perovskite benefited the energy level alignment between the perovskite and Spiro-OMeTAD and then the hole extraction. In addition, the defect density of the perovskite active layer was significantly reduced after the introduction of δ-CsPbI$_3$; the PCE of PSCs based on this anion-barrier modification then increased from 19.62% to 21.21%.

Finally, due to the inhibition of iodide diffusion by the formed anion-barrier, the conductivity of Spiro-OMeTAD and even the silver electrode was reserved. After monitoring for about 1200 h under dark conditions with 15%–25% RH, the PCE of the optimized device can still maintain about 88.2% of its initial device, showing excellent device stability. This work demonstrates that the *in situ* synthesis of the anion barrier layer is a multi-effect strategy for ion diffusion and contact interface.

Author contributions

W. Zeng, C. Xu, S. Zhang and Q. Song conceived the work, and discussed the results. W. Zeng and Z. Jiang carried out the experiment. W. Zeng, X. He, L. Lai, J. You, G. Xu and H. Bian participated in characterization and analysis. Z. Jiang, X. He, C. Xu and Z. Dai contributed to the sketches. All authors discussed the results and contributed to the manuscript.

Data availability

The authors confirm that the data supporting the findings of this study are available within the article [and/or its ESI†].

Conflicts of interest

There are no conflicts to declare.

Acknowledgements

References

1 C. Y. Xu, W. Hu, G. Wang, L. B. Niu, A. M. Elseman, L. P. Liao, Y. Q. Yao, G. B. Xu, L. Luo, D. B. Liu, G. D. Zhou, P. Li and Q. L. Song, Coordinated optical matching of a texture interface made from demixing blended polymers for high performance inverted perovskite solar cells, *ACS Nano*, 2020, **14**, 196–203.

2 G. Wang, L. P. Liao, A. M. Elseman, Y. Q. Yao, C. Y. Lin, W. Hu, D. B. Liu, C. Y. Xu, G. D. Zhou, P. Li, L. J. Chen, J. J. Han, X. D. Yang, R. Wu, X. Rao and Q. L. Song, An internally photoemitted hot carrier solar cell based on organic-inorganic perovskite, *Nano Energy*, 2020, **68**, 104383.

3 Y. H. Deng, S. Xu, S. Chen, X. Xiao, J. J. Zhao and J. S. Huang, Defect compensation in formamidinium–caesium perovskites for highly efficient solar mini-modules with improved photostability, *Nat. Energy*, 2021, **6**, 633–641.

4 W. Pan, P. Chen, S. Zhu, R. He, Q. Zheng, F. Cao, Z. Lan, J. Wu, W. Sun and Y. Li, Enhanced performance of perovskite solar cells via a bilateral electron-donating passivator as a molecule bridge, *Inorg. Chem. Front.*, 2023, **10**, 5734–5744.

5 Q. Zhou, B. B. Liu, Y. Chen, D. Q. Ma, X. Han, D. M. He, Z. F. Zhang, H. Yang, L. M. Ding, J. Feng, J. H. Yi, C. Chen and J. Z. Chen, Pre-embedded multisite chiral molecules realize bottom-up multilayer manipulation toward stable and efficient perovskite solar cells, *Adv. Funct. Mater.*, 2023, 2315064.

6 National Renewable Energy Laboratory Best research-cell efficiency chart, https://www.nrel.gov/pv/cell-efficiency.html.

7 B. Duan, Y. Ren, Y. Xu, W. Chen, Q. Ye, Y. Huang, J. Zhu and S. Dai, Identification and characterization of a new intermediate to obtain high quality perovskite films with hydrogen halides as additives, *Inorg. Chem. Front.*, 2017, **4**, 473–480.

8 M. Wang, L. Fan, W. Lü, Q. Sun, X. Wang, F. Wang, J. Yang, H. Liu and L. Yang, Interior/interface modification of textured perovskite for enhanced photovoltaic outputs of planar solar cells by an in situ growth passivation technology, *ACS Appl. Mater. Interfaces*, 2021, **13**, 39689–39700.

9 G. Tumen-Ulzii, C. Qin, D. Klotz, M. R. Leyden, P. Wang, M. Auffray, T. Fujihara, T. Matsushima, J. W. Lee, S. J. Lee, Y. Yang and C. Adachi, Detrimental effect of unreacted PbI$_2$ on the long-term stability of perovskite solar cells, *Adv. Mater.*, 2020, **32**, e1905035.

10 F. Z. Liu, Q. Dong, M. K. Wong, A. B. Djurišić, Z. Ren, Q. Shen, C. Surya, W. K. Chan, J. Wang, C. Liao, H. Li, K. Shih, C. Wei, H. Su and J. Dai, Is excess PbI$_2$ beneficial for perovskite solar cell performances, *Adv. Energy Mater.*, 2016, **6**, 1502206.

11 J. Liang, X. Hu, C. Wang, C. Liang, C. Chen, M. Xiao, J. Li, C. Tao, G. Xing, R. Yu, W. Ke and G. Fang, Origins and influences of metallic lead in perovskite solar cells, *Joule*, 2022, **6**, 816–833.

12 W. Zhang, S. Pathak, N. Sakai, T. Stergiopoulos, P. K. Nayak, N. K. Noel, A. A. Haghighirad, V. M. Burlakov, D. W. Quilettes, A. Sadhanala, W. Li, L. Wang, D. S. Ginger, R. H. Friend and H. J. Snaith, Enhanced optoelectronic quality of perovskite thin films with hypophosphorous acid for planar heterojunction solar cells, *Nat. Commun.*, 2015, **6**, 10030.

13 Y. Ma, G. Han, M. Yang, M. Guo, Y. Xiao, Y. Guo and W. Hou, Inhibiting Li$^+$ migration by thenoyltrifluoroacetone toward efficient and stable perovskite solar cells, *Inorg. Chem. Front.*, 2023, **10**, 2294–2303.

14 J. F. Zhang, X. Q. Jiang, X. T. Liu, X. Guo and C. Li, Maximizing merits of undesirable δ–FAPbI$_3$ by constructing yellow/black heterophase bilayer for efficient and stable

5144 | *Inorg. Chem. Front.*, 2024, **11**, 5137–5146

This journal is © the Partner Organisations 2024

perovskite photovoltaics, *Adv. Funct. Mater.*, 2022, **32**, 2204642.

15 D. Y. Li, Y. L. Huang, G. L. Wang, Q. Lian, R. Shi, L. Zhang, X. Wang, F. Gao, W. Kong, B. Xu, C. Cheng and S. Li, Boosting the performance of MA-free inverted perovskite solar cells via multifunctional ion liquid, *J. Mater. Chem. A*, 2021, **9**, 12746–12754.

16 J. C. Xi, Y. Y. Wu, W. J. Chen, Q. Li;, J. Li, Y. Shen, H. Chen, G. Xu, H. Yang, Z. Chen, N. Li, J. Zhu, Y. Li and Y. Li, Cross-linkable molecule in spatial dimension boosting water-stable and high-efficiency perovskite solar cells, *Nano Energy*, 2021, **93**, 106846.

17 D. Di Girolamo, N. Phung, F. U. Kosasih, F. Di Giacomo, F. Matteocci, J. A. Smith, M. A. Flatken, H. Köbler, S. H. Turren Cruz, A. Mattoni, L. Cinà, B. Rech, A. Latini, G. Divitini, C. Ducati, A. Di Carlo, D. Dini and A. Abate, Ion migration–induced amorphization and phase segregation as a degradation mechanism in planar perovskite solar cells, *Adv. Energy Mater.*, 2020, **10**, 2000310.

18 D. Wei, F. Ma, R. Wang, S. Dou, P. Cui, H. Huang, J. Ji, E. Jia, X. Jia, S. Sajid, A. M. Elseman, L. Chu, Y. Li, B. Jiang, J. Qiao, Y. Yuan and M. Li, Ion-migration inhibition by the cation-π interaction in perovskite materials for efficient and stable perovskite solar cells, *Adv. Mater.*, 2018, **30**, 1707583.

19 J. Carrillo, A. Guerrero, S. Rahimnejad, O. Almora, I. Zarazua, E. Mas-Marza, J. Bisquert and G. Garcia-Belmonte, Ionic reactivity at contacts and aging of methyl-ammonium lead triiodide perovskite solar cells, *Adv. Energy Mater.*, 2016, **6**, 1502246.

20 H. Lee and C. Lee, Analysis of ion-diffusion-induced interface degradation in inverted perovskite solar cells via restoration of the Ag electrode, *Adv. Energy Mater.*, 2018, **8**, 1702197.

21 Y. Kato, L. K. Ono, M. V. Lee, S. Wang, S. R. Raga and Y. Qi, Silver iodide formation in methyl ammonium lead iodide perovskite solar cells with silver top electrodes, *Adv. Mater. Interfaces*, 2015, **2**, 1500195.

22 Z. Qin, Y. Chen, X. Wang, N. Wei;, X. Liu, H. Chen, Y. Miao and Y. Zhao, Zwitterion–functionalized SnO_2 substrate induced sequential deposition of black–phase $FAPbI_3$ with rearranged PbI_2 residue, *Adv. Mater.*, 2022, **34**, 2203143.

23 M. K. A. Mohammed, 21.4% efficiency of perovskite solar cells using BMImI additive in the lead iodide precursor based on carbon nanotubes/TiO_2 electron transfer layer, *Ceram. Int.*, 2020, **46**, 27647–27654.

24 F. Ke, C. X. Wang, C. J. Jia, N. R. Wolf, J. Yan, S. Niu, T. P. Devereaux, H. I. Karunadasa, W. L. Mao and Y. Lin, Preserving a robust $CsPbI_3$ perovskite phase via pressure-directed octahedral tilt, *Nat. Commun.*, 2021, **12**, 461.

25 T. Ye, L. Pan, Y. Yang, Q. Liang, Y. Lu, M. Sui, D. Golberg and X. Wang, Synthesis of highly-oriented black $CsPbI_3$ microstructures for high-performance solar cells, *Chem. Mater.*, 2020, **32**, 3235–3244.

26 R. J. Sutton, M. R. Filip, A. A. Haghighirad, N. Sakai, B. Wenger, F. Giustino and H. J. Snaith, Cubic or ortho-rhombic revealing the crystal structure of metastable black-phase $CsPbI_3$ by theory and experiment, *ACS Energy Lett.*, 2018, **3**, 1787–1794.

27 L. Wang, M. Shahiduzzaman, E. Y. Muslih, M. Nakano, M. Karakawa, K. Takahashi, K. Tomita, J. M. Nunzi and T. Taima, Double-layer CsI intercalation into an $MAPbI_3$ framework for efficient and stable perovskite solar cells, *Nano Energy*, 2021, **86**, 106135.

28 P. Y. Wang, Q. Jiang, Y. Zhao, Y. Chen, Z. Chu, X. Zhang, Y. Zhou and J. You, Synergistic improvement of perovskite film quality for efficient solar cells via multiple chloride salt additives, *Sci. Bull.*, 2018, **63**, 726–731.

29 S. Chi, S. Yang, Y. Wang, D. Li, L. Zhang, L. Fan, F. Wang, X. Liu, H. Liu, M. Wei, J. Yang and L. Yang, Break through the steric hindrance of ionic liquids with carbon quantum dots to achieve efficient and stable perovskite solar cells, *ACS Appl. Mater. Interfaces*, 2023, **15**, 48304–48315.

30 S. L. Tang, Y. Peng, Z. Zhu, J. Zong, L. Zhao, L. Yu, R. Chen and M. Li, Simultaneous bulk and surface defect passivation for efficient inverted perovskite solar cells, *J. Phys. Chem. Lett.*, 2022, **13**, 5116–5122.

31 G. S. Yuan, S. W. Feng, Q. Yang, F. L. Yi, X. Y. Li, Y. Q. Yuan, C. J. Wang and H. J. Yan, Promoting charge separation in a composite of δ-$CsPbI_3$ and covalent organic frameworks, *J. Mater. Chem. C*, 2023, **11**, 7570–7574.

32 Q. Li, Y. H. Xiang, R. Zheng, C. Li, K. K. Ren, B. Yao, H. T. Xu, S. Y. Liu, Y. S. Tan and Z. B. Fang, Improvement in efficiency and reproducibility for $FAPbI_3$ solar cells with rapid crystallization, *Energy Fuels*, 2023, **37**, 791–797.

33 J. A. Yang, A. D. Xiao, L. S. Xie, K. Liao, X. Deng, C. Li, A. Wang, Y. Xiang, T. Li and F. Hao, Precise control of PbI_2 excess into grain boundary for efficacious charge extraction in off-stoichiometric perovskite solar cells, *Electrochim. Acta*, 2020, **338**, 135697.

34 L. Collins, M. Ahmadi, T. Wu, B. Hu, S. V. Kalinin and S. Jesse, Breaking the time barrier in kelvin probe force microscopy: fast free force reconstruction using the G-mode platform, *ACS Nano*, 2017, **11**, 8717–8729.

35 Z. W. Gao, Y. Wang, Z. Y. Jiang, B. Hu, B. Xu and W. C. H. Choy, Multifunctional ion–lock interface layer achieved by solid–solid contact approach for stabilizing perovskite solar cells, *Adv. Funct. Mater.*, 2022, **36**, 2200473.

36 C. Caddeo, D. Marongiu, S. Meloni, A. Filippetti, F. Quochi, M. Saba and A. Mattoni, Hydrophilicity and water contact angle on methylammonium lead iodide, *Adv. Mater. Interfaces*, 2018, **6**, 1801173.

37 W. Hu, C. Y. Xu, L. B. Niu, A. M. Elseman, G. Wang, D. B. Liu, Y. Q. Yao, L. P. Liao, G. D. Zhou and Q. L. Song, High open-circuit voltage of 1.134 V for inverted planar perovskite solar cells with sodium citrate-doped PEDOT:PSS as a hole transport layer, *ACS Appl. Mater. Interfaces*, 2019, **11**, 22021–22027.

38 M. Yu, L. Chen, G. Li, C. Xu, C. Luo, M. Wang, G. Wang, Y. Yao, L. Liao, S. Zhang and Q. Song, Effect of guanidinium chloride in eliminating O^{2-} electron extraction barrier on a SnO_2 surface to enhance the efficiency of perovskite solar cells, *RSC Adv.*, 2020, **10**, 19513–19520.

This journal is © the Partner Organisations 2024

Inorg. Chem. Front., 2024, **11**, 5137–5146 | **5145**

39 S. Béchu, M. Ralaiarisoa, A. Etcheberry and P. Schulz, Photoemission spectroscopy characterization of halide per-ovskites, *Adv. Energy Mater.*, 2020, **10**, 1904007.

40 W. J. Chen, D. Li, S. S. Chen, S. Liu, Y. Shen, G. Zeng, X. Zhu, E. Zhou, L. Jiang, Y. Li and Y. Li, Spatial distri-bution recast for organic bulk heterojunctions for high–performance all–inorganic perovskite/organic integrated solar cells, *Adv. Energy Mater.*, 2020, **10**, 2000851.

41 S. Asgharizadeh, S. Khesali Azadi and M. Lazemi, Understanding the pathways toward improved efficiency in MXene-assisted perovskite solar cells, *J. Mater. Chem. C*, 2022, **10**, 1776–1786.

42 W. Q. Zeng, X. F. He, H. Y. Bian, P. Guo, M. Wang, C. Xu, G. Xu, Y. Zhong, D. Lu, Z. Sofer, Q. L. Song and S. Zhang, Multi-functional strategy: Ammonium citrate-modified SnO_2 ETL for efficient and stable perovskite solar cells, *ACS Appl. Mater. Interfaces*, 2022, **14**, 43975–43986.

43 Y. X. Zhong, C. M. Li, G. B. Xu, C. Xu, J. Dong, D. Liu, D. Lu, J. You, C. Gao and Q. Song, Collaborative strengthen-ing by multi-functional molecule 3-thiophenboric acid for efficient and stable planar perovskite solar cells, *Chem. Eng. J.*, 2022, **436**, 135134.

44 D. Li, L. He, Z. Pang, F. Wang, L. Fan, X. Liu, M. Wei and L. Yang, Anchoring grain boundary via aminated carbon nanotubes to achieve efficient and stable perovskite solar cells, *Sol. RRL*, 2022, **6**, 2200297.

45 H. Wu, J. Qiu, J. Wang, Y. Wen, Q. Wang, Z. Long, D. Zhou, Y. Yang and D. Wang, The dual-defect passivation role of lithium bromide doping in reducing the nonradiative loss in $CsPbX_3$ (X = Br and I) quantum dots, *Inorg. Chem. Front.*, 2021, **8**, 658–668.

46 Y. Zhao, Y. Zhao, W. Zhou, Q. Li, R. Fu, D. Yu and Q. Zhao, In situ cesium modification at interface enhances the stabi-lity of perovskite solar cells, *ACS Appl. Mater. Interfaces*, 2018, **10**, 33205–33213.

47 Y. H. Chen, N. X. Li, L. G. Wang, L. Li, Z. Xu, H. Jiao, P. Liu, C. Zhu, H. Zai, M. Sun, W. Zou, S. Zhang, G. Xing, X. Liu, J. Wang, D. Li, B. Huang, Q. Chen and H. Zhou, Impacts of alkaline on the defects property and crystallization kinetics in perovskite solar cells, *Nat. Commun.*, 2019, **10**, 1112.

48 X. F. Cao, J. Guo, Y. G. Luan, J. Zhuang, G. Niu, H. Liu and J. Wang, Defect reduction by anthraquinone-modified graphdiyne quantum dots for efficient perovskite solar cells, *2D Mater.*, 2021, **8**, 044010.

49 N. Shibayama, H. Kanda, T. W. Kim, H. Segawa and S. Ito, Design of BCP buffer layer for inverted perovskite solar cells using ideal factor, *APL Mater.*, 2019, **7**, 031117.

50 Z. Wang, L. X. Zeng, C. L. Zhang, Y. Lu, S. Qiu, C. Wang, C. Liu, L. Pan, S. Wu, J. Hu, G. Liang, P. Fan, H. J. Egelhaaf, C. J. Brabec, F. Guo and Y. Mai, Rational interface design and morphology control for blade–coating efficient flexible perovskite solar cells with a record fill factor of 81%, *Adv. Funct. Mater.*, 2020, **30**, 2001240.

51 W. Q. Zeng, Z. Z. Jiang, X. F. He, L. M. Lai, J. Y. You, G. B. Xu, H. Y. Bian, C. Y. Xu, Z. J. Dai, S. Zhang and Q. L. Song, *Inorg. Chem. Front.*, 2024, DOI: 10.1039/d4qi00327f.

5146 | *Inorg. Chem. Front.*, 2024, **11**, 5137–5146

This journal is © the Partner Organisations 2024